Size-Dependent Brittle-to-Ductile Transition in Silica Glass Nanofibers

Junhang Luo,[†,#] Jiangwei Wang,[†,#] Erik Bitzek,[‡,§,#] Jian Yu Huang,[∥] He Zheng,[†] Limin Tong,[⊥] Qing Yang,[⊥] Ju Li,*[‡] and Scott X. Mao*[†]

[†]Department of Mechanical Engineering & Materials Science, University of Pittsburgh, Pittsburgh, Pennsylvania 15261, United States

[‡]Department of Nuclear Science and Engineering and Department of Materials Science and Engineering, Massachusetts Institute of Technology, 77 Massachusetts Avenue, Cambridge, Massachusetts 02139, United States

[§]Department of Materials Science and Engineering, Institute I, Friedrich-Alexander-Universität Erlangen-Nürnberg (FAU), 91058 Erlangen, Germany

[⊥]State Key Laboratory of Modern Optical Instrumentation, Department of Optical Engineering, Zhejiang University, Hangzhou 310027, China

S *Supporting Information*

ABSTRACT: Silica (SiO_2) glass, an essential material in human civilization, possesses excellent formability near its glass-transition temperature ($T_g > 1100$ °C). However, bulk SiO_2 glass is very brittle at room temperature. Here we show a surprising brittle-to-ductile transition of SiO_2 glass nanofibers at room temperature as its diameter reduces below 18 nm, accompanied by ultrahigh fracture strength. Large tensile plastic elongation up to 18% can be achieved at low strain rate. The unexpected ductility is due to a free surface affected zone in the nanofibers, with enhanced ionic mobility compared to the bulk that improves ductility by producing more bond-switching events per irreversible bond loss under tensile stress. Our discovery is fundamentally important for understanding the damage tolerance of small-scale amorphous structures.
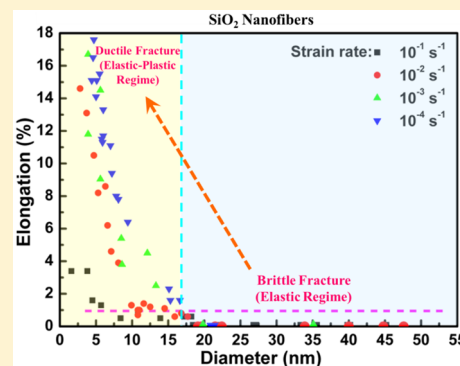
KEYWORDS: *Brittle-to-ductile transition, silica glass, in situ transmission electron microscopy, glass surface, plasticity*

"Happiness and glass break easily"—despite proverbial brittleness it has been long argued that fracture in glass could be accompanied by plastic flow processes at room temperature.[1−3] In previous studies, plastic flow has been well-established during the deformation of glass under compressive stress.[2,4,5] Under tensile stress, however, brittle fracture is commonly observed in glasses at room temperature.[6,7] Recently, the nucleation, growth and coalescence of nanosized cavities were detected in glasses at the front of a crack during its propagation, as revealed by both experiments[8,9] and molecular dynamics (MD) simulations.[10−12] These discoveries may suggest the existence of a plastic zone in front of the crack tip and thus the occurrence of plastic flow at the nanoscale. However, this issue remains controversial[6,13,14] in view of the classic work on the "brittle" fracture of glasses conducted by Griffith.[15]

Recently, an electron-beam-assisted superplastic deformability was discovered in amorphous silica (SiO_2) nanoparticles and nanowires at room temperature, where the irradiation damage from electron beam can facilitate bond-switching and plastic flow.[16] Electron-beam irradiation can also result in the densification of SiO_2 spheres via irradiation-assisted atomic rearrangement in the silica network, inducing hardening.[17] Although pronounced tensile elongation can be achieved in

SiO_2 nanowires above room temperature (around 60 °C),[18] the effect of temperature on the plastic flow of nanoscale SiO_2 is unknown, and could be greatly promoted by the small sample size.[19,20] Tensile testing of SiO_2 nanofibers was also conducted at room temperature under optical microscopy,[18] however, clear evidence of plastic flow is lacking due to low resolution. Thus, room temperature plasticity of SiO_2 at the nanoscale, especially without electron beam irradiation, remains underexplored. Recently, a critical size for specimens was postulated, below which structures would become "flaw-insensitive".[21,22] For silica fibers, the critical diameter is of the order of 0.5−1 nm. The fracture behavior of silica nanowires should therefore still be dominated by defects, and brittle fracture is expected to take place down to fibers only a few atoms in diameter.

Here we present a combined experiment/simulation study on the deformation of nanosized SiO_2 fibers. We reveal a size-dependent strengthening and brittle-to-ductile transition in SiO_2 nanofibers, namely the onset of ultrahigh strength and tensile ductility when the diameter is reduced to below 18 nm.
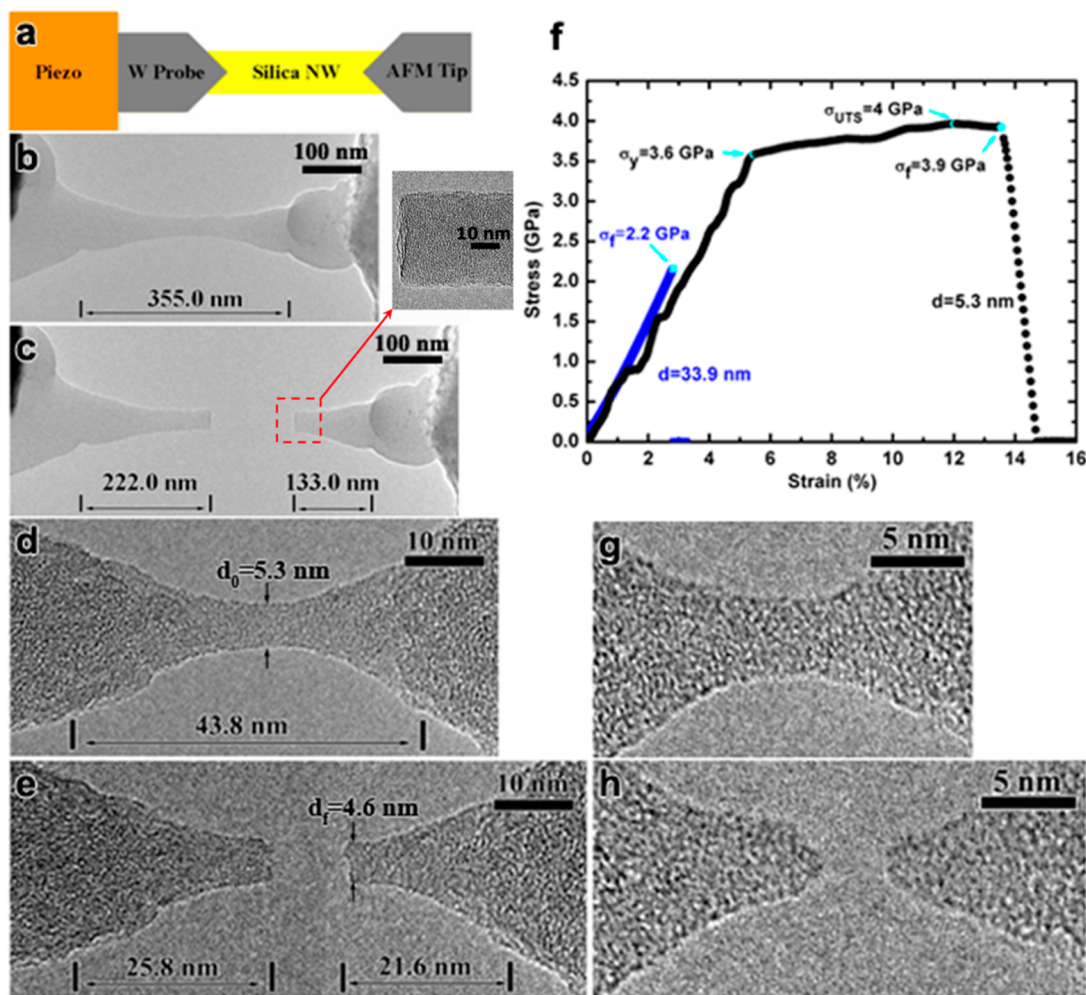
Figure 1. Deformation behavior of SiO_2 nanofibers with different diameters. (a) Schematics of the experimental setup. (b, c) Morphology of a 33.9 nm SiO_2 nanofiber before (b) and after (c) fracture. The nanofiber was deformed at a strain rate of 3.3×10^{-2} s^{-1}. (d, e) Morphology of a 5.3 nm SiO_2 nanofiber before (d) and after (e) fracture. The nanofiber was deformed at a strain rate of 1.1×10^{-2} s^{-1}. (f) Strain−stress curves of the two nanofibers shown in parts b−e. (g, h) Localized necking occurred in a 4.0 nm nanofiber at a strain rate of 5.2×10^{-4} s^{-1}.

Atomistic simulations suggest that the ductility of SiO_2 nanofibers is mediated by surface processes, in which abundant surface sites catalyze more bond-switching events which relax stresses by shear deformation rather than bond breaking. Our conclusions in many ways corroborate recent findings of enhanced molecular mobility and reduced glass transition temperature in near-surface regions (sub-10 nm) in polymeric and organic glasses,[23−25] but with an added ingredient of large applied stress, and manifestation on tensile ductility.

Figure 1a shows a schematics of the in situ tensile testing. Dog-bone shaped samples with diameters ranging from 1 to 40 nm were *in situ* prepared inside the TEM. In the tensile tests, a displacement controlled deformation was realized by a piezo controller, providing strain rates between 10^{-1} and 10^{-4} s^{-1}. After the fracture of the SiO_2 nanofibers, the microstructures near the fracture zone were further analyzed by high resolution TEM (HRTEM) to check for crystallization. Detailed information about the experiments and MD simulations can be found in the Methods and our other works.[26−29]

Since without e-beam amorphous SiO_2 nanofibers with diameters larger than 50 nm always exhibit brittle fracture under tensile loading,[30,31] we focus here only on amorphous SiO_2 nanofibers with diameters less than 50 nm. Figure 1parts

b,c and d,e show the tensile deformation of two SiO_2 nanofibers with diameters of the 33.9 and 5.3 nm, respectively. Tensile testing was conducted under beam-blank condition. The 33.9 nm SiO_2 nanofiber shows a clearly brittle failure without observable plastic elongation, as demonstrated by the measured nanofiber length and the flat fracture surfaces perpendicular to the loading direction in Figure 1c. The stress−strain curve of 33.9 nm SiO_2 nanofiber further confirms its brittle nature, in which limited elastic deformation (∼2.5%) occurred before the sudden fracture, accompanied by a low fracture strength of 2.2 GPa (Figure 1f). Supporting Information, Figure S1 presents another example of the brittle fracture of a SiO_2 nanofiber with a diameter of 18.7 nm, along with a higher fracture strength and elastic strain limit (∼4.8%). The Young's modulus of those SiO_2 nanofibers are about 77.6 GPa (Supporting Information, Figure S1), close to that of bulk SiO_2.[1] The observed brittle fracture of SiO_2 nanofibers are in contrast to the large plasticity of SiO_2 nanofibers when deformed under e-beam irradiation,[16] even though smaller sample sizes are employed in the current study (The large surface-to-volume ratio of smaller sample is expected to promote plastic flow). However, as the diameter further decreases, some plastic elongation with clear ductile fracture characteristics are observed. Figure 1d−f show an

example for the ductile fracture of a 5.3 nm SiO$_2$ nanofiber. It is observed that the gauge length of this nanofiber increases from originally 43.8 to 47.4 nm after fracture (Figure 1e), corresponding to a permanent plastic elongation of 8.2%. Notably, an apparent diameter decrease (from the initial 5.3 to 4.6 nm) and rough fracture surfaces are also captured after its fracture (Figure 1e), suggesting that significant plastic flow occurs in the tensile deformation of the 5.3 nm SiO$_2$ nanofiber.

This notion of ductile failure under electron beam-blank condition is further confirmed by its stress−strain curve in Figure 1f. An important feature in the stress−strain curve of the 5.3 nm nanofiber is the significant plastic flow occurring before the fracture, a direct evidence of ductile deformation. A permanent plastic elongation of ∼8.5% is obtained after fracture, consistent with the value obtained from TEM imaging. It is also noted that some strain hardening occurs after the initial yielding (∼3.6 GPa) of the 5.3 nm nanofiber and results in an ultimate tensile strength (UTS) of ∼4 GPa. Like other ductile materials, the strain hardening is followed by a slight softening under further loading, indicating that the fracture of SiO$_2$ glass can proceed via ductile necking at nanoscale. Figure 1h shows the fracture morphology of a 4.0 nm SiO$_2$ nanofiber, which demonstrates the occurrence of significant necking at the fracture zone. Similar ductile features and hardening behavior are also observed in other SiO$_2$ nanofibers with small diameters (Supporting Information, Figure S2). As demonstrated above, the distinct mechanical behaviors of SiO$_2$ nanofibers with different diameters suggest a clear brittle-to-ductile transition as the fiber diameter is reduced down to tens of nanometers.

To further confirm the notion of brittle-to-ductile transition in nanosized SiO$_2$ glass, 72 individual nanofibers with diameters between 1 to 50 nm (Supporting Information, Table S1) were tested at different strain rates. The statistics of fracture strengths and tensile elongations of these nanofibers are summarized in Figure 2, parts a and b, respectively. In Figure 2a, the fracture strengths of SiO$_2$ nanofibers show a strong increase with decreasing diameter, similar to the size effect on strength in other crystal and glass systems.[32] As the diameter goes down to ∼1 nm, an ultrahigh strength of 13.2 GPa was achieved, close to the theoretical strength of silica (∼16 GPa). Figure 2b shows that SiO$_2$ nanofibers with large diameters experienced negligible plastic elongation before their fracture (much smaller than 1%, as indicated by the dashed line), consistent with the results shown in Figure 1b,c. However, high plastic elongation can be achieved in SiO$_2$ nanofiber with the reduction of diameter (Figure 2b). A transition from brittle fracture to ductile failure occurs when the diameter is decreased below 18 nm. For diameters below 18 nm, the plastic elongation of SiO$_2$ nanofiber shows a net increase with the decrease of nanofiber diameter (Figure 2b). Pronounced plastic elongations up to 18% are achieved in nanofibers with diameters ∼5 nm at room temperature (Figure 2b). Accompanying the improved plastic elongation is the change of fracture morphology, from the flat fracture surfaces in nanofibers with diameters larger than 18 nm to significant diameter decrease and necking in nanofibers with diameters less than 18 nm, as shown in Figure 1 and Supporting Information, Figures S1−3. Note that the maximum room temperature plastic elongation of SiO$_2$ nanofibers obtained in our experiments is smaller than the ones (over 100%) pulled by heating up bimetallic sheets in a hot stage to a temperature ∼60 °C,[18] even though similar strain rates are employed in both
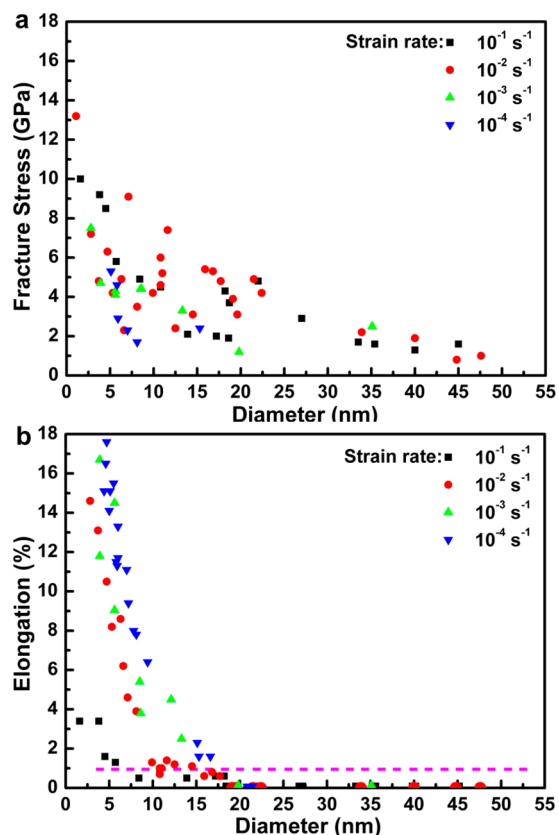
Figure 2. Size and strain-rate dependence of (a) fracture strength and (b) maximum plastic elongation of SiO$_2$ nanofibers. The dashed line in part b indicates a reference line of 1%.

studies, which can be attributed to the thermal effect that greatly benefits the plastic flow at nanoscale.

Figure 2 also indicates that the ductility and fracture strength of SiO$_2$ nanofibers are not only size dependent but also strain-rate dependent. In the brittle fracture regime, the mechanical behavior of SiO$_2$ nanofibers is insensitive to the strain rate. However, it becomes highly sensitive to the strain rate once in the ductile size regime. Below the transition size of 18 nm, a higher plastic elongation can be achieved in SiO$_2$ nanofibers when deforming at low strain rate, accompanied by lower fracture strength. Although the fracture strength shows some scatter when analyzed with respect to the strain-rate dependence, there is a general tendency of lower fracture stresses at slower strain rates. Moreover, strain rate also influences the critical size for brittle-to-ductile transition in SiO$_2$ nanofibers. According to the 1% elongation criterion (dashed line in Figure 2b), the transition is found to occur at 5 nm at a strain rate of 10^{-1} s^{-1}, while it is 18 nm at a strain rate of 10^{-4} s^{-1}. This indicates that a creep-like strain rates (10^{-4} s^{-1} and below) are beneficial for achieving high ductility in our materials, and thus diffusive creep deformation mechanism could be important.

We note that free surfaces are usually perceived as the preferred initiation sites of cracks in the deformation of SiO$_2$ fibers with very large size, leading to brittle fracture.[15,33] However, in our beam-blank experiments, the free surface appears to have a "beneficial" effect on the ductility of SiO$_2$ nanofibers. To understand the abnormal room-temperature tensile ductility of SiO$_2$ nanofibers, molecular dynamics (MD) simulations were performed. MD simulations reveal that the plastic deformation of ultrathin SiO$_2$ nanofibers is controlled by

the delayed formation of voids, which effectively postpones the localized and thus global fracture, as shown in Figure 3. Figure
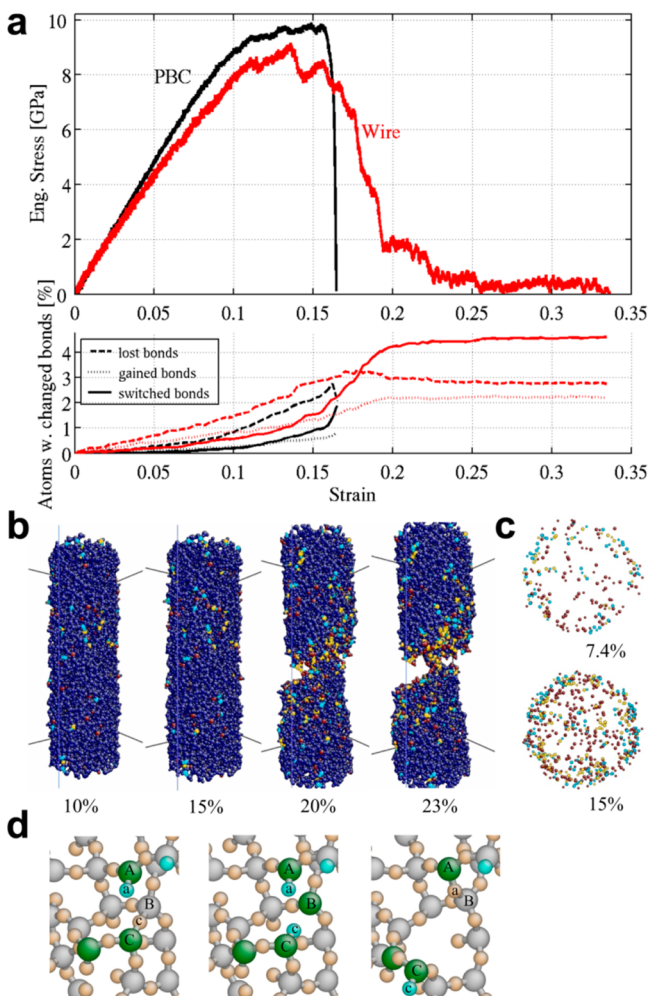
Figure 3. Molecular dynamics simulations of the tensile behavior of SiO_2 glass (Vashishta potential). (a) Stress−strain responses of the wire and the periodic boundary conditions (PBC) sample together with the bond-switching statistics. (b) Deformation snapshots of the wire at different strains (blue atoms have no change in bonding topology, cyan atoms have gained bonding partners, yellow atoms have switched bonds, red atoms have lost bonds). (c) Top view of the wire, showing only atoms with changes in bonding topology (same color code as in part b). (d) Example of a bond-switching process involving the migration of nonbridging O-defect and the rotation of a partially unbonded silica tetrahedron (around C) (color coding according to the coordination number).

3a shows the stress−strain curve and the statistics of bond-change events during the deformation of a 4.5 nm SiO_2 nanofiber. Upon pulling, some Si−O bonds will break and create void-like volumes (Figure 3a). However, if dangling oxygen bonds are present, these can quickly move to the under-coordinated Si atom forming a new Si−O bond (Figure 3). We identify this ionic motion pattern as a bond-switching process. MD reveals that there is a surface-plasticized region where bond-switching dominates (Figure 3c). In this near-surface region of enhanced plasticity, the occurrence of bond-switching events exceeds the irreversible bond loss, and thus flaws can be somewhat blunted. Once the surface affected region spans the nanofiber, the entire fiber can deform plastically as a whole with

less coordination loss per strain sustained, as shown in Figure 1. The existence of a surface-plasticized layer in SiO_2 glass may also solve the puzzle of why the fracture seems to proceed by the nucleation and coalescence of cavities when monitored at the intersection of the crack tip with a macroscopic surface,[8,34] whereas analysis of fractography inside the sample does not reveal any signs of ductility.[6]

The mechanism of shear relaxation by bond-switching is generally analogous to the one proposed for viscous flow in silica at high temperatures,[35] void coalescence under hydro-static tension[36] and superplasticity under irradiation.[16] However, in contrast to those three scenarios, bonding switching in nanofibers is mainly surface assisted. The influence of the surface on the plastic deformation is two-fold: first, the missing bonding constraints at the surface lead to an increased flexibility of the partly unbonded silica tetrahedra (as seen, e.g., in the rotation of a tetrahedron in Figure 3d). This increased flexibility allows for the transportation of nonbridging oxygen atoms close to under-coordinated silicon atoms, thereby healing preexisting or deformation-induced surface damage. Second, the presence of under-coordinated atoms at the surface catalyzes bond-switching and thus plastic deformation. Such more efficient relaxation[23−25] and densification near freshly created surfaces corroborates similar finding of ultrastable and ultradense organic glass grown by vapor deposition[37] where there was a moving surface. As shown in Figure 3c, the atoms involved in the plastic deformation are also mostly situated close to the surface of the nanofiber. As the sample size increases, the effect from the surfaces becomes reduced. The cavities or crack-nuclei in the interior of the sample have no way out but to expand/coalesce under the high stress, quickly exceeding the critical size and developing into a crack that is attracted to the surface. Therefore, the observed resistance to fracture and the ability to sustain large plastic flow is a "size effect" due to the extraordinarily large surface-to-volume ratio and surface-assisted shear-diffusion transformations[38,39] which reduce damage accumulation due to a fast surface-mediated repair mechanism, which under experimental conditions most probably will also benefit from surface ionic diffusion.

High strain rate can promote the room-temperature strength and tensile ductility of both crystalline and amorphous materials.[40−42] However, in our experiments, the ductility of SiO_2 nanofibers show a reversed behavior, that is improved ductility under low strain rate, though their strengths follow the similar trend as other materials. The abnormal strain-rate dependence of the ductility of SiO_2 nanofibers can be attributed to its unique deformation mechanism of "surface diffusion".[20,43] The plastic flow of SiO_2 nanofibers is mainly mediated by the surface-plasticized region, in which bond changes occur frequently and result in the annihilation of cavities or crack-nuclei that were generated by the deformation. However, the occurrence of bond-switching requires some relaxation time for the bond rotation and reconnection. The deformation under low strain rate provides enough time for the surface diffusion assisted bond-rotation and damage repair processes, which benefits the ductile deformation. The ductility also benefits from the stabilization of superplastic flow by a high strain-rate sensitivity m,[44] as an ideal diffusive creep should give $m = 1$ due to the small activation volume of the atomic processes of diffusion.[32]

Although the tensile tests of SiO_2 nanofibers were conducted under beam-blank conditions, some electron beam irradiation occurred during the sample preparation and imaging process,
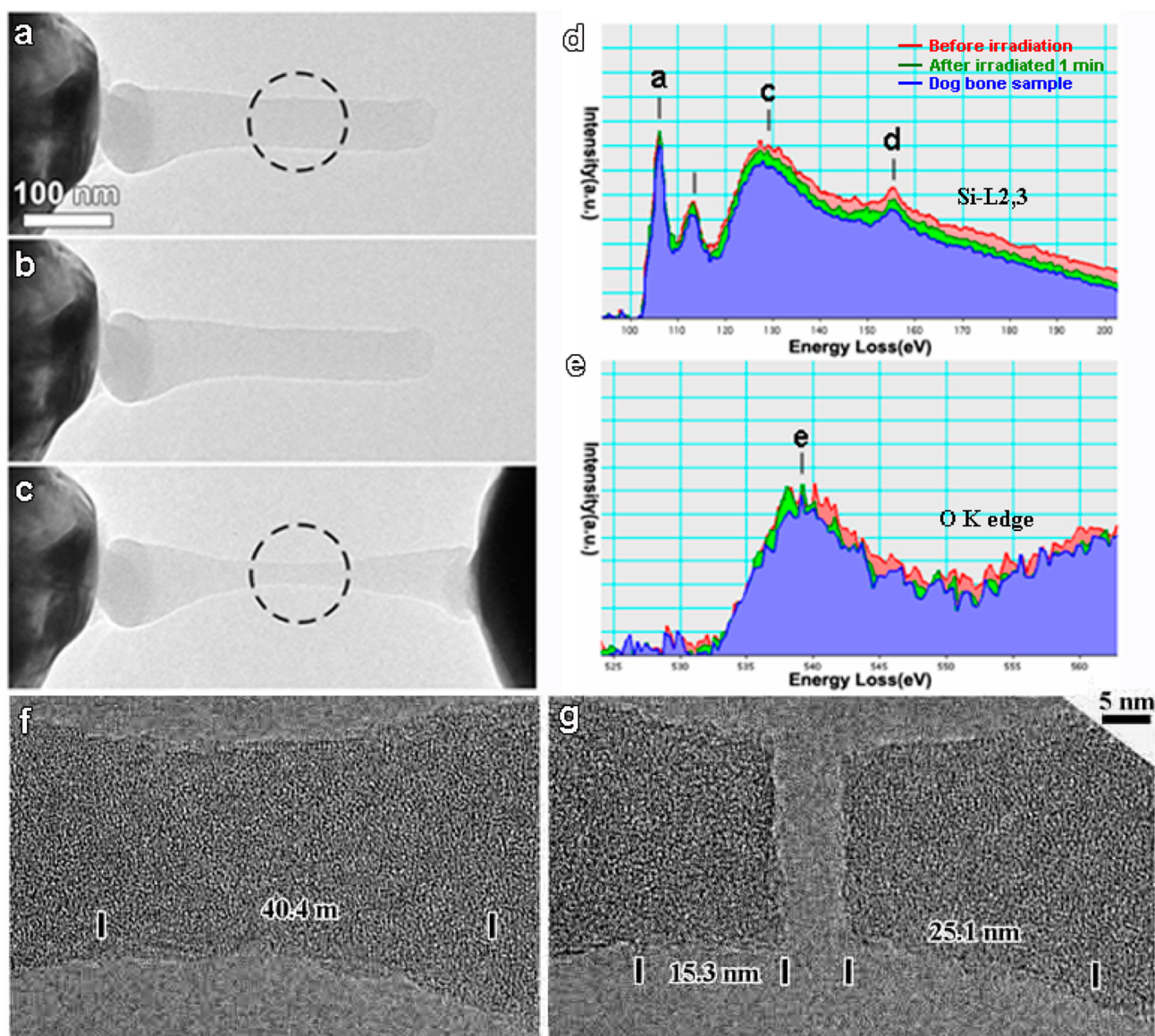
Figure 4. Morphologies, EELS spectra and postirradiation deformation of SiO_2 nanofibers. (a−e) Morphologies and EELS spectra of SiO_2 nanofibers for different sample preparation protocols. The areas where the EELS were recorded are marked by the dotted circles. (a, b) Morphology of a 56 nm nanofiber before and after 1 min irradiation, respectively. (c) As-prepared dog-bone sample with a diameter of 24.6 nm made from the 56 nm nanofiber. (d, e) Corresponding EELS spectra of Si-L2,3 edge and O−K edge. The EELS peak energy is (a) 106.0, (b) 112.9, (c) 128.8, (d) 155.2, and (e), 539.0 eV. (f, g) Postirradiation tensile experiment on a 21.1 nm SiO_2 nanofiber. The tensile testing was conducted at a strain rate of $2.5 \times 10^{-4} \ s^{-1}$. (f) Image of the nanofiber before 2 min beam irradiation. (g) Fracture of the nanofiber after the tensile test.

which might affect the plastic deformation. The displacement threshold energy for amorphous SiO_2 is ∼25 eV,[45] while our experiments were conducted with 300 kV electron beam that gives maximum 53 eV to O and 30 eV to Si in direct impact. To determine the influences of prior beam irradiation on the composition and deformation behaviors of SiO_2 nanofibers, electron energy loss spectroscopy (EELS) and postirradiation tensile experiments were further performed. Figure 4a−e shows the morphologies and EELS spectra of a SiO_2 nanofiber before and after the sample preparation under electron beam. The diameter of the pristine nanofiber is 56 nm. After the irradiation under a beam current density of ∼2.5×10^{-3} A/cm^2 for 1 min (similar to the irradiation condition of sample preparation process), no change in morphology is observed (Figure 4a,b). Finally, a dog-bone nanofiber sample of 24.6 nm is prepared from the initial thick nanofiber (Figure 4c). The corresponding

EELS spectra of Si-L2,3 edge and O−K edge under these three conditions are presented in Figure 4d and 4e, respectively. The lack of any observable difference between the Si-L2,3 edge and O−K edge of these three samples suggests that the beam irradiation in sample preparation does not change the composition of the SiO_2 nanofiber measurably. Moreover, the lack of a peak at ∼531 eV indicates that no detectable molecular oxygen (O_2) was generated during the irradiation.[46] As a result, the dog-bone sample should remain pure SiO_2.

Some dangling bonds and oxygen vacancies/interstitials could be introduced by the irradiation in sample preparation and imaging processes,[16] but they should have negligible effect on the deformation. SiO_2 nanofibers with the diameter as large as 129 nm can deform via superplastic flow when exposed to electron beam irradiation (Supporting Figure S4). However, the beam-blank experiments demonstrate that nanofibers with

diameters larger than 18 nm are intrinsically brittle, as suggested by both stress−strain curve and fracture morphologies (Figures 1 and 2 and Supporting Figure S1). These comparative results indicate that the defects generated by the irradiation in sample preparation and imaging processes have negligible contribution to the brittle-to-ductile transition of SiO_2 nanofibers. To further confirm this point, a preirradiated silica nanofiber of 21.1 nm is tested under beam-blank condition, as shown in Figure 4f,g. The SiO_2 nanofiber was irradiated for 2 min under an electron beam with the current density of ~2.5×10^{-3} A/cm^2, same as the one used in other sample preparations. After the preirradiation, tensile testing was performed under beam-blank condition. Notably, the preirradiated SiO_2 nanofiber still keep the brittle fracture with a flat fracture surface (Figure 4g), consistent with the one deformed without beam illumination. A previous study showed that the electron beam induced damage can be totally healed in CaO-Al$_2$O$_3$−SiO$_2$ glass once the beam was turned off for 2 min.[46] Studies on the irradiation of amorphous SiO_2 showed that irradiation-induced oxygen atoms can further bond with the silicon dangling bonds (E' centers),[47] forming peroxy radicals and links.[48,49] As such, the degree of recovery of radiation damage should depend on the number of oxygen atoms that locked into defect bonding configurations in the network, which reduces the number of nonbridging sites for reabsorption of the silicon. In the current experiments, a very weak beam was used to facilitate fabrication of the sample, and no molecular oxygen (O_2) was generated during the sample preparation process (Figure 4a−e). Thus, the irradiation-induced silicon dangling bonds can easily reconnect with their neighboring nonbridging oxygen atoms once the beam is turned off, leading to the formation of new Si−O bonds. As a result, the saturated silicon dangling bonds may not be enough to facilitate the plastic flow of preirradiated SiO_2 nanofibers with large diameter (e.g., the sample in Figure 4f−g) when deformed without irradiation, due to the recovery of irradiation damage. Therefore, it can be concluded that the irradiation in sample preparation and imaging processes has limited influence on the deformation of SiO_2 nanofiber, and the size-dependent brittle-to-ductile transition revealed in our experiments is conceptually different from the concept of irradiation-induced plasticity.[16]

The large number of tests on nanofibers prepared by the same procedure show the robustness of the observed size-dependent brittle-to-ductile transition. However, it is well-known that the details of the sample production as well as the thermal, mechanical and environmental history of glass specimens have significant effects on their mechanical behavior[3,50,51] both in experiments and in simulations. In how far the present observations can be generalized to glass fibers produced by completely different routes therefore remains an open question. Differences in surface structure and thermo-mechanical history could for example explain the different strength values reported in ref 52. Similarly, simulation samples generated by different methods can show significantly different fracture behavior.[50] The casting procedure of Yuan and Huang[50] for example produces significantly fewer surface defects compared to our charge-conserving cutting method. However, the scarcity of surface defects in their simulation precludes the observation of significant bond-switching events in the limited time scale (~nanoseconds) of MD simulations. The use of samples with more surface defects overestimates the rate of bond-switching, however allows to observe the migration of defects and the formation of the plasticized zone

within time scales accessible by MD. The mechanistic insights gleaned from the simulations, namely, that surfaces contain more defects than the bulk, and that surface bonds are less constrained than bonds in the bulk and defects can thus be transported over a certain distance, leading to a surface-affected plasticized zone in which stress concentrations can be diminished by bond-switching rather than leading to bond breaking, are however independent of the experimental or simulation details. It is therefore to be expected that size-dependent ductility is a general feature of silica nanofibers. The magnitude of this effect will however certainly depend on the details of the fiber preparation.

In conclusion, our results show that in the presence of free surfaces, silica glass can be ductile at length scales around 10 nm due to surface-assisted shear-diffusion transformations[38,39,53] with reduced damage accumulation due to expedited repair by surface diffusion.[23−25,37] Alternatively one may say the glass transition temperature of the near-surface region is significantly reduced[23−25] to allow significant plastic forming at room temperature. A significant brittle-to-ductile transition occurs in silica nanofibers as the size scales down below 18 nm. The plasticity in such small volumes is attributed to the increase in bond-switching events per irreversible bond loss in the surface-affected zone. Their ductility, high strength (close to the theoretical strength[30,54]) and high elastic-strain limit opens up a wide range of applications utilizing nanoscale glass with damage tolerance in elastic strain engineering and harsh conditions.[6,28,29,32] Our results should also be relevant for understanding friction and tribology, because the mechanical energy dissipation ability of a surface glassy layer is much greater than what may be expected before. For example, microelectromechanical systems (MEMS) based on silicon always have thermally grown oxide on top, of a few to few tens of nanometers thick. Our results indicate that such SiO_2 overlayer should have mechanical behavior far different from normal glasses[23−25] and is much more damage-tolerant than macroscale glasses.

Methods. *Sample Preparation and Nanomechanical Testing.* All the silica glass nanofibers used in this study were directly drawn from large silica glass via a two-step process: self-modulated taper-drawing and fiber-drawing under TEM. In the first step, highly uniform SiO_2 nanofibers with diameters down to 50 nm were fabricated by a self-modulated taper-drawing process, a schematic diagram of which is shown in Supporting Information, Figure S8. A standard SiO_2 fiber (e.g., SMF-28 from Corning Inc.) was heated and drawn to a micrometer diameter wire, which was wrapped on the tip of a tapered sapphire fiber for further drawing to a smaller nanofiber. Then, a 90° elastic bend around the taper of the SiO_2 fiber was introduced by holding the SiO_2 fiber parallel to the sapphire taper and tautening the connected microfiber between the taper of the SiO_2 fiber. A tensile force perpendicular to the sapphire and SiO_2 fiber was produced this way and used for self-modulation. As the microfiber elongated and the diameter scaled down, the bend loosens and the bending center moved toward the thin end of the taper, resulting in smaller forces for drawing thinner wires. The as-prepared SiO_2 nanofibers have uniform diameters and lengths over a hundred millimeter. A typical scanning electron microscopy (SEM) image of a SiO_2 nanofiber is shown in Supporting Information, Figure S9a.

In the second step, a dog-bone SiO_2 nanofiber tensile sample was further drawn from the prefabricated nanowire inside a FEI Tecnai F30 field emission gun (FEG) TEM, operated at 300 kV

with a point-to-point resolution of about 0.19 nm. The SiO_2 nanofiber prepared in the first step was used to further fabricate the dog-bone sample. A manipulator was applied to control a STM tip with silver paint to pick up a SiO_2 nanofiber with the length of several micrometers under an optical microscope. Then the nanofiber was inserted into one end of a TEM-STM platform, and another STM tip with bulk silica was used as another end of the platform. After being transferred into the TEM, all operations were performed carefully in a low dose mode (5×10^{-4} to 2.5×10^{-3} A/cm^2) to minimize beam exposure. After the STM tip with bulk silica touched the SiO_2 nanofiber, the electron beam of 1 A/cm^2 was focused at the contacting area to sinter them together, while the center of the nanofiber was not exposed to the beam. Then the focused beam was moved away to a blank area and expanded to a very low intensity ($\sim 5 \times 10^{-4}$ to 2.5×10^{-3} A/cm^2) for observation. The next step was to use image shift to move the desired cutting point to the center of the fluorescence screen. Usually a 200−500 nm segment was cut from the original nanofiber, which was loaded into a Nanofactory TEM atomic force microscopy (AFM) platform for mechanical testing. After the short SiO_2 segment touched the silica on the AFM tip, the electron beam was used to weld them together. Finally, the dog-bone samples (diameter ranging in 1 to 40 nm) were prepared from the short SiO_2 segment via a thinning process of in situ drawing inside TEM under electron beam illumination ($\sim 2.5 \times 10^{-3}$ A/cm^2), similar to the taper-drawing process in the first step for making the thick fibers. Electron beam was used to facilitate the material flow and thus the drawing process, however, special care was taken during the sample preparation to minimize possible irradiation damage. Usually, the thinning process occurred at the center of the thick sample, and as such a dog-bone sample was obtained after the drawing. Before tensile testing, the sample shape, size and surface condition were checked under TEM and only nanofibers with smooth surfaces were chosen for the mechanical tests. Supporting Information, Figure S9b shows an as-prepared dog-bone sample with a diameter of 28.2 nm, along with the HRTEM image in Supporting Information, Figure S9c. Supporting Information, Figure S9d is the HRTEM image of the broken part of the dog-bone sample. The two HRTEM images clearly show that no crystallization occurs in the sample before and after fracture. To determine the composition and the shape of the cross-section, the electron energy dispersive spectra (EDS) and line scanning were acquired, as shown in Supporting Figure Information, S9e−h. We did the EDS at position 1 and the line scanning at position 2. The EDS spectrum consists of only silicon and oxygen, and a quantitative analysis reveals that the ratio of O to Si is close to 1.96 (Supporting Information, Figure S9f), a little less than the stoichiometric ratio but within the EDS error range. The EDS intensity profiles Supporting Information, Figure S9g−h suggests that the dog-bone sample has a circular cross section.

Finally, all tensile tests were performed at room temperature inside TEM, using a Nanofactory TEM-AFM platform. The spring constant k of the AFM cantilever used for nano-mechanical testing is 4.4 N m^{-1}. To accurately monitor the deformation, the nanofiber with clear surface features or obvious markers were chose as the initial gauge length. The minimum diameter in the gauge length of nanofiber was measured for the stress calculation. During the nanomechanical testing, various strain rates were realized by a piezo controller and the deformation forces F were obtained based on the deflection of the AFM tip. To minimize the possible irradiation damage, all tensile testings were conducted under beam-blank conditions, within which the electron beam was only used to image the initial and final configurations of deformation. Engineering stresses were then calculated by $\sigma = 4F/(\pi D^2)$, where D is the minimum nanofiber diameter. The total plastic elongation of SiO_2 nanofibers were obtained by $\varepsilon_{total} = (l_f - l_0)/l_0$, where l_0 and l_f are the sample length under the initial and fractured states, respectively. During deformation, the load−displacement curves were recorded by the control software.

Simulation Methods. Molecular dynamics simulations of uniaxial tensile deformation at a constant strain rate of 10^9 s^{-1} at 300 K were performed on two amorphous silica samples: a wire of a diameter $d = 4.5$ nm and a length $l = 11$ nm with periodic boundary conditions along the wire axis, and a rectangular sample of dimensions $5.5 \times 5.5 \times 11$ nm^3 under periodic boundary conditions in all directions. Two interaction potentials were used: the original silica three-body potential by Vashishta et al.[55] cut off, shifted and smoothed at $r_c = 0.8$ nm according to the procedure detailed in ref 56, and the two-body potential by van Beest, Kramer, and van Santen (BKS)[57] which was cut off and shifted at $r_c = 1.5$ nm using a smooth cutoff function.

The $5.5 \times 5.5 \times 11$ nm^3 bulk sample was constructed from a crystobalite crystal following the stepwise cooling procedure laid out in ref 58: the sample was equilibrated for 90000 steps at 5000, 4000, 3000, 2500, 2000, 1500, and 1000 K. Between these constant temperature simulations, the sample was cooled with a rate of 166 K/ps. In all simulations, 0 MPa pressure was maintained by a Berendsen barostat and a time step of 0.5 fs was used. Energy minimization was performed on the 500 K sample followed by equilibration at 300 K, again at 0 MPa pressure. This procedure corresponds to an effective cooling rate of 13 K/ps. With the Vashishta potential, the so obtained sample has a density of $\rho = 2.42$ (2.2) g/cm^3 and 0K elastic constants (experimental values from[59] in brackets): Young's modulus $E = 109$ (73−74) GPa, shear modulus $G = 44$ (31) GPa, and bulk modulus $B = 61$ (31−38) GPa, leading to Poisson's ratio of $\nu = 0.21 (0.17−0.18)$. The BKS sample has the following properties: $\rho = 2.38$ (2.2) g/cm^3, $E = 71$ (73−74) GPa, $G = 31.7$ (31) GPa, $B = 36.6$ (31−38) GPa. With these values the Poisson ratio can be calculated to $\nu = 0.16$ (0.17−0.18).

From the relaxed sample, the wire was cut out, taking care that the overall charge neutrality was maintained. It is important to note that as the wire was created from the bulk sample, the inside of the wire shares the same microstructure as the bulk sample, and both samples were free of apparent flaws. The wire was again relaxed and equilibrated at 300 K. MD simulations were carried out using the DLPOLY package using the Berendsen thermostat with a time step of 1 fs and the smoothed particle mesh Ewald method for calculating the Coulomb interactions (real space cutoff 1.05 nm and accuracy of 10^{-6}). In the bulk simulations, the length of the box vectors orthogonal to the tensile direction is controlled by the Berendsen barostat to maintain uniaxial stress conditions.

The number of atoms with lost, switched or gained bonds was determined by the differences in bonding topology between the actual configuration and the reference configuration at zero strain. Each atom is identified by its unique number ID. Atoms are considered to have lost bonds when their coordination number z (the number of atoms within the nearest neighbor shell of radius $r = 0.2016$ nm) has decreased

with respect to the reference configuration. Atoms which gain a bond show respectively an increase of z. Atoms with switched bonds have the same z as in the reference configuration, however, at least one nearest neighbor has a different ID than in the reference configuration.

■ ASSOCIATED CONTENT

ⓈSupporting Information

The Supporting Information is available free of charge on the ACS Publications website at DOI: 10.1021/acs.nano-lett.5b03070.

Additional experimental and MD simulation results about the deformation of SiO_2 nanofibers and image preparation (PDF)

■ AUTHOR INFORMATION

Corresponding Authors

*(J.L.) E-mail: liju@mit.edu.

*(S.X.M.) E-mail: sxm2@pitt.edu.

Present Address

∥(J.Y.H.) 8915 Hampton Ave NE, Albuquerque, New Mexico 87122, USA

Author Contributions

#These authors contributed equally to this work.

Notes

The authors declare no competing financial interests.

■ ACKNOWLEDGMENTS

■ REFERENCES

(1) Ferreira Nascimento, M. L.; Zanotto, E. D. Physics and chemical of glass. *Phys. Chem. Glasses - Eur. J. Glass Sci. Technol. Part B* **2007**, *48*, 201−217.

(2) Marsh, D. M. Plastic Flow and Fracture of Glass. *Proc. R. Soc. London, Ser. A* **1964**, *282*, 33−43.

(3) Kurkjian, C. R.; Gupta, P. K.; Brow, R. K. The strength of silicate glasses: what do we know, what do we need to know? *Int. J. Appl. Glass Sci.* **2010**, *1*, 27−37.

(4) Hagan, J. T. Shear Deformation under Pyramidal Indentations in Soda-Lime Glass. *J. Mater. Sci.* **1980**, *15*, 1417−1424.

(5) Lacroix, R.; Kermouche, G.; Teisseire, J.; Barthel, E. Plastic deformation and residual stresses in amorphous silica pillars under uniaxial loading. *Acta Mater.* **2012**, *60*, 5555−5566.

(6) Guin, J. P.; Wiederhorn, S. M. Fracture of silicate glasses: Ductile or brittle? *Phys. Rev. Lett.* **2004**, *92*, 215502.

(7) Lawn, B. R.; Hockey, B. J.; Wiederhorn, S. M. Atomically Sharp Cracks in Brittle Solids - an Electron-Microscopy Study. *J. Mater. Sci.* **1980**, *15*, 1207−1223.

(8) Celarie, F.; et al. Glass breaks like metal, but at the nanometer scale. *Phys. Rev. Lett.* **2003**, *90*, 075504.

(9) Marliere, C.; et al. Crack fronts and damage in glass at the nanometre scale. *J. Phys.: Condens. Matter* **2003**, *15*, S2377−S2386.

(10) Chen, Y. C.; et al. Interaction of voids and nanoductility in silica glass. *Phys. Rev. Lett.* **2007**, *99*, 155506.

(11) Van Brutzel, L.; Rountree, C. L.; Kalia, R. K.; Nakano, A.; Vashishta, P. Dynamic Fracture Mechanisms in Nanostructured and Amorphous Silica Glasses Million-Atom Molecular Dynamics Simulations. *MRS Online Proc. Libr.* **2002**, *703*, V3.9.

(12) Rountree, C. L.; et al. A unified study of crack propagation in amorphous silica: Using experiments and simulations. *J. Alloys Compd.* **2007**, *434*, 60−63.

(13) Fett, T.; et al. Finite element analysis of a crack tip in silicate glass: No evidence for a plastic zone. *Phys. Rev. B: Condens. Matter Mater. Phys.* **2008**, *77*, 174110.

(14) Lopez-Cepero, J. M.; Wiederhorn, S. A.; Fett, T.; Guin, J. P. Do plastic zones form at crack tips in silicate glasses? *Int. J. Mater. Res.* **2007**, *98*, 1170−1176.

(15) Griffith, A. A. The Phenomena of Rupture and Flow in Solids. *Philos. Trans. R. Soc., A* **1921**, *221*, 163−198.

(16) Zheng, K.; et al. Electron-beam-assisted superplastic shaping of nanoscale amorphous silica. *Nat. Commun.* **2010**, *1*, 24.

(17) Mačković, M.; Niekiel, F.; Wondraczek, L.; Spiecker, E. Direct observation of electron-beam-induced densification and hardening of silica nanoballs by in situ transmission electron microscopy and finite element method simulations. *Acta Mater.* **2014**, *79*, 363−373.

(18) Yue, Y.; Zheng, K. Strong strain rate effect on the plasticity of amorphous silica nanowires. *Appl. Phys. Lett.* **2014**, *104*, 231906.

(19) Yue, Y.; et al. Crystalline Liquid and Rubber-Like Behavior in Cu Nanowires. *Nano Lett.* **2013**, *13*, 3812−3816.

(20) Sun, J.; et al. Liquid-like pseudoelasticity of sub-10-nm crystalline silver particles. *Nat. Mater.* **2014**, *13*, 1007−1012.

(21) Gao, H.; Ji, B.; Jäger, I. L.; Arzt, E.; Fratzl, P. Materials become insensitive to flaws at nanoscale: lessons from nature. *Proc. Natl. Acad. Sci. U. S. A.* **2003**, *100*, 5597−5600.

(22) Gao, H.; Chen, S. Flaw tolerance in a thin strip under tension. *J. Appl. Mech.* **2005**, *72*, 732−737.

(23) Fakhraai, Z.; Forrest, J. A. Measuring the surface dynamics of glassy polymers. *Science* **2008**, *319*, 600−604.

(24) Ellison, C. J.; Torkelson, J. M. The distribution of glass-transition temperatures in nanoscopically confined glass formers. *Nat. Mater.* **2003**, *2*, 695−700.

(25) Yang, Z. H.; Fujii, Y.; Lee, F. K.; Lam, C. H.; Tsui, O. K. C. Glass Transition Dynamics and Surface Layer Mobility in Unentangled Polystyrene Films. *Science* **2010**, *328*, 1676−1679.

(26) Wang, J.; et al. Near-ideal theoretical strength in gold nanowires containing angstrom scale twins. *Nat. Commun.* **2013**, *4*, 1742.

(27) Wang, J. W.; et al. Atomic-scale dynamic process of deformation-induced stacking fault tetrahedra in gold nanocrystals. *Nat. Commun.* **2013**, *4*, 2340.

(28) Wang, J.; et al. Strong Hall−Petch Type Behavior in the Elastic Strain Limit of Nanotwinned Gold Nanowires. *Nano Lett.* **2015**, *15*, 3865−3870.

(29) Wang, J.; et al. In situ atomic-scale observation of twinning-dominated deformation in nanoscale body-centred cubic tungsten. *Nat. Mater.* **2015**, *14*, 594−600.

(30) Brambilla, G.; Payne, D. N. The Ultimate Strength of Glass Silica Nanowires. *Nano Lett.* **2009**, *9*, 831−835.

(31) Ni, H.; Li, X. D.; Gao, H. S. Elastic modulus of amorphous SiO_2 nanowires. *Appl. Phys. Lett.* **2006**, *88*, 043108.

(32) Zhu, T.; Li, J. Ultra-strength materials. *Prog. Mater. Sci.* **2010**, *55*, 710−757.

(33) Bartenev, G. M. The structure and strength of glass fibers. *J. Non-Cryst. Solids* **1968**, *1*, 69−90.

(34) Bonamy, D.; et al. Nanoscale damage during fracture in silica glass. *Int. J. Fract.* **2006**, *140*, 3−14.

(35) Mott, N. F. The viscosity of vitreous silicon dioxide. *Philos. Mag. B* **1987**, *56*, 257−262.

(36) Pradeep, N.; et al. Ductility at the nanoscale: Deformation and fracture of adhesive contacts using atomic force microscopy. *Appl. Phys. Lett.* **2007**, *91*, 203114.

(37) Swallen, S. F.; et al. Organic glasses with exceptional thermodynamic and kinetic stability. *Science* **2007**, *315*, 353−356.

(38) Mao, Y.; Li, J.; Lo, Y.-C.; Qian, X.; Ma, E. Stress-driven crystallization via shear-diffusion transformations in a metallic glass at very low temperatures. *Phys. Rev. B: Condens. Matter Mater. Phys.* **2015**, *91*, 214103.

(39) Li, W. B.; Rieser, J. M.; Liu, A. J.; Durian, D. J.; Li, J. Deformation-driven diffusion and plastic flow in amorphous granular pillars. *Phys. Rev. E* **2015**, *91*, 062212.

(40) Wang, J.; et al. Tensile Deformation Behaviors of Cu-Ni Alloy Processed by Equal Channel Angular Pressing. *Adv. Eng. Mater.* **2010**, *12*, 304−311.

(41) Dao, M.; Lu, L.; Shen, Y.; Suresh, S. Strength, strain-rate sensitivity and ductility of copper with nanoscale twins. *Acta Mater.* **2006**, *54*, 5421−5432.

(42) Peng, C.; et al. Strain rate dependent mechanical properties in single crystal nickel nanowires. *Appl. Phys. Lett.* **2013**, *102*, 083102.

(43) Tian, L.; Li, J.; Sun, J.; Ma, E.; Shan, Z.-W. Visualizing size-dependent deformation mechanism transition in Sn. *Sci. Rep.* **2013**, *3*, 2113.

(44) Hutchinson, J. W.; Neale, K. W. INFLUENCE OF STRAIN-RATE SENSITIVITY ON NECKING UNDER UNIAXIAL TENSION. *Acta Metall.* **1977**, *25*, 839−846.

(45) Jiang, N.; Silcox, J. Electron irradiation induced phase decomposition in alkaline earth multi-component oxide glass. *J. Appl. Phys.* **2002**, *92*, 2310−2316.

(46) Mkhoyan, K.; Silcox, J.; Ellison, A.; Ast, D.; Dieckmann, R. Full recovery of electron damage in glass at ambient temperatures. *Phys. Rev. Lett.* **2006**, *96*, 205506.

(47) Griscom, D. L. E′ center in glassy Si O 2: Microwave saturation properties and confirmation of the primary Si 29 hyperfine structure. *Phys. Rev. B: Condens. Matter Mater. Phys.* **1979**, *20*, 1823.

(48) Friebele, E.; Griscom, D.; Stapelbroek, M.; Weeks, R. Fundamental defect centers in glass: the peroxy radical in irradiated, high-purity, fused silica. *Phys. Rev. Lett.* **1979**, *42*, 1346.

(49) Tsai, T.; Griscom, D. Experimental evidence for excitonic mechanism of defect generation in high-purity silica. *Phys. Rev. Lett.* **1991**, *67*, 2517.

(50) Yuan, F.; Huang, L. Molecular dynamics simulation of amorphous silica under uniaxial tension: From bulk to nanowire. *J. Non-Cryst. Solids* **2012**, *358*, 3481−3487.

(51) Yuan, F.; Huang, L. Brittle to ductile transition in densified silica glass. *Sci. Rep.* **2014**, *4*, 5035.

(52) Brambilla, G.; Payne, D. N. *Nano Lett.* **2009**, *9*, 831−835.

(53) Mao, Y. W.; Li, J.; Lo, Y. C.; Qian, X. F.; Ma, E. Stress-driven crystallization via shear-diffusion transformations in a metallic glass at very low temperatures. *Phys. Rev. B: Condens. Matter Mater. Phys.* **2015**, *91*, 214103.

(54) Zhao, P. Y.; Li, J.; Wang, Y. Z. Extended defects, ideal strength and actual strengths of finite-sized metallic glasses. *Acta Mater.* **2014**, *73*, 149−166.

(55) Vashishta, P.; Kalia, R. K.; Rino, J. P.; Ebbsjo, I. Interaction Potential for SiO_2 - a Molecular-Dynamics Study of Structural Correlations. *Phys. Rev. B: Condens. Matter Mater. Phys.* **1990**, *41*, 12197−12209.

(56) Vashishta, P.; Kalia, R. K.; Nakano, A.; Li, W.; Ebbsjö, I. Molecular dynamics methods and large-scale simulations of amorphous materials. *Amorphous Insulators and Semiconductors* **1996**, *33*, 151−213.

(57) Van Beest, B.; Kramer, G.; Van Santen, R. Force fields for silicas and aluminophosphates based on ab initio calculations. *Phys. Rev. Lett.* **1990**, *64*, 1955−1958.

(58) Nakano, A.; Kalia, R. K.; Vashishta, P. First sharp diffraction peak and intermediate-range order in amorphous silica: finite-size effects in molecular dynamics simulations. *J. Non-Cryst. Solids* **1994**, *171*, 157−163.

(59) Shackelford, J. F.; Alexander, W. *CRC materials science and engineering handbook*; CRC press: Boca Raton, FL, 2000.

Size-Dependent Brittle-to-Ductile Transition in Silica Glass Nanofibers

Junhang Luo[1,#], Jiangwei Wang[1,#], Erik Bitzek[2,3,#], Jian Yu Huang[4], He Zheng[1], Limin Tong[5], Qing Yang[5], Ju Li[2,*], Scott X. Mao[1,*]

[1]*Department of Mechanical Engineering & Materials Science, University of Pittsburgh, Pittsburgh, Pennsylvania 15261, USA*

[2]*Department of Nuclear Science and Engineering and Department of Materials Science and Engineering, Massachusetts Institute of Technology, 77 Massachusetts Avenue, Cambridge, Massachusetts 02139, USA*

[3]*Department of Materials Science and Engineering, Institute I, Friedrich-Alexander-Universität Erlangen-Nürnberg (FAU), 91058 Erlangen, Germany*

[4]*8915 Hampton Ave NE, Albuquerque, New Mexico 87122, USA*

[5]*State Key Laboratory of Silicon Materials, Zhejiang University, Hangzhou 310027, China*

Supplementary Information

1. Additional results of the tensile tests
2. Additional molecular dynamics simulation results
3. Images about sample preparation

1. Additional results of the tensile tests

The beam was blanked during the tensile tests to exclude the irradiation on the deformation behavior of SiO_2 nanofiber. The morphologies of pristine and fractured nanofibers were captured to reveal the fracture mode. Supporting Figure S1 shows the deformation and loading-unloading response of a SiO_2 nanofiber with the diameter of 18.7 nm. The nanofiber was firstly deformed via loading-unloading test and then pulled again until fracture. The SiO_2 nanofiber of 18.7 nm shows a typical brittle fracture, as demonstrated by the flat fracture surface (Supporting Figure S1c) and the stress-strain curve (Supporting Figure S1e). The fracture strength of 18.7 nm SiO_2 nanofiber was about 3.7 GPa, with a Young's modulus of 77.6 GPa (Supporting Figure S1d-e). Before the sudden fracture, the maximum elastic strain occurred in the 18.7 nm nanofiber was 4.8%, which is over 1.5 times that of the 33.9 nm diameter nanofiber (Figure 1f in the main text). The increase in strength and elastic strain limit can be attributed to the size-dependent strengthening.

Supporting Figure S2 show an example about the ductile fracture of a 4.7 nm nanofiber with 18% tensile elongation. The nanofiber is deformed under the strain rate of 2.8×10^{-4} s^{-1}. Significant diameter shrunk and localized necking is observed in the fracture morphologies, confirming the ductile fracture mode. Supporting Figure S3 shows the fracture morphologies of SiO_2 nanofibers under higher strain rates. The fracture of 22.4 nm under a high strain rate of 4.4×10^{-2} s^{-1} shows a shear fracture feature (Supporting Figure S3a), while a localized necking is observed in 2.8 nm nanofiber under the strain rate of 4.7×10^{-2} s^{-1}, similar to the fracture behaviors under low strain rate (Figure 1g-h in the main text).

To reveal the effects of electron beam irradiation on the deformation, a SiO_2 nanofiber with the diameter up to 128.8 nm were deformed under the strain rate of 2.7×10^{-4} s^{-1}. A superplastic deformation was observed before the fracture of this 128.8 nm SiO_2 nanofiber (Supporting Figure S4), in contrast to the brittle behavior of 33.9 nm and 18.7 nm nanofibers when deformed under beam-blank conditions (Figure 1b-c in the main text and Supporting Figure S1), even though the diameters are much smaller in the beam-blank deformation cases. The control experiments suggest that the beam irradiation has negligible influences on the deformation.

Moreover, in our experiments, 72 individual SiO_2 nanofibers with different diameters were fabricated and tested under various deformation strain rate at room temperature. Their diameters, deformation conditions, fracture strengths and plastic elongations are summarized in Supporting Table S1 and plotted in Figure 2 in the main text. The engineering fracture strength was calculated by $4\Delta F/\pi d_0^2$, where ΔF refers to the force at the fracture point and d_0 is the initial diameter of the nanofiber. The plastic elongation was calculated by $(L_f - L_0)/L_0$, where L_0 and L_f are the initial and final (i.e. determined after fracture) gauge length of the nanofiber.
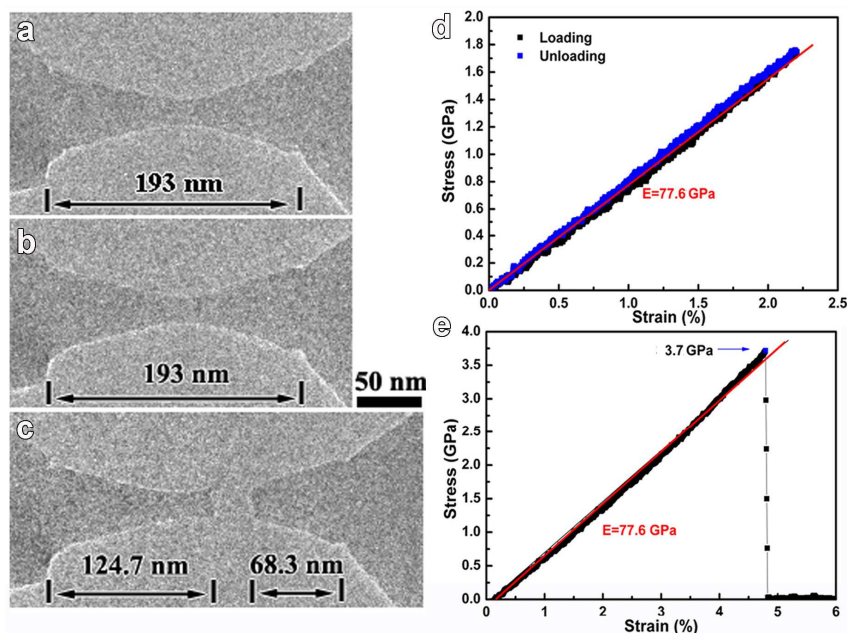
Figure S1 Mechanical tests on the SiO$_2$ nanofiber with the diameter of 18.7 nm. **a**, **b** and **c** are images of the nanofiber before, after cycle loading and final fracture; **d** and **e** are the strain-stress curves for the cycle loading and tensile test.
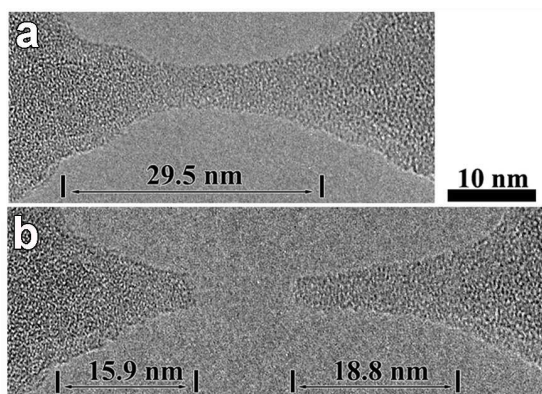
Figure S2 Ductile fracture of a 4.7 nm SiO$_2$ nanofiber with an elongation of ~18%. **a,** the pristine nanofiber and **b**, the fractured nanofiber after tensile deformation at a strain rate of 2.8×10^{-4} s^{-1}.
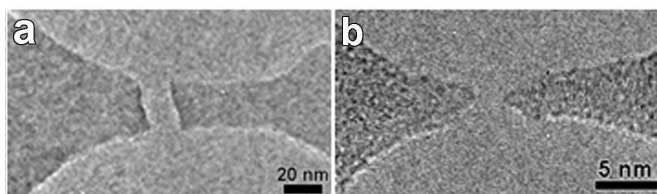
Figure S3 Fracture morphologies of SiO$_2$ nanofibers under higher strain rates. **a,** a shear fracture of a 22.4 nm nanofiber at a strain rate of 4.4×10^{-2} s^{-1}; **b,** localized necking of a 2.8 nm nanofiber at a strain rate of 4.7×10^{-2} s^{-1}.
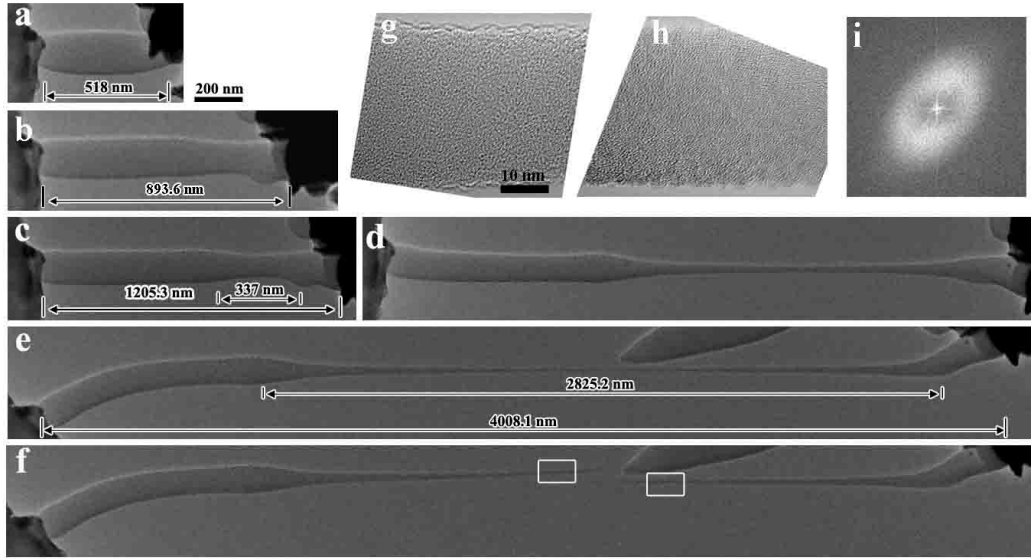
Figure S4. In situ tensile elongation of a 128.8 nm SiO_2 nanofiber at strain rate of 2.7×10^{-4} s^{-1}. (a) t=0 min, tensile test beginning. (b) t=22 min, local thinning happened at the place near the contacting area of the STM probe side. (c) t=69 min, a dog-bond-shaped sample; (d) t=212 min, the dog-bond-shaped sample uniformly elongated along the wire axis; (e) t=246 min, the nanowire just before failure; (f) Failure of the nanowire. (g) and (h) are HRTEM images of the white framed regions in (f). (i) FFT of (h).

Table S1 Summary of fracture strengths and plastic elongations of SiO_2 nanofibers

Sample	Initial diameter (nm) d_0	Elongation (%) $(L_f - L_0)/L_0$	Fracture stress (GPa) $4\Delta F/d_0^2$	Strain rate (s^{-1})
NW1-1	1.6	3.4	10.0	6.1×10^{-2}
NW1-2	3.8	3.4	9.2	1.2×10^{-1}
NW1-3	4.5	1.6	8.5	1.7×10^{-1}
NW1-4	5.7	1.3	5.8	1.6×10^{-1}
NW1-5	8.4	0.5	4.9	5.0×10^{-1}
NW1-6	10.8	0.9	4.5	1.1×10^{-1}
NW1-7	13.9	0.5	2.1	1.3×10^{-1}
NW1-8	17.2	0.6	2.0	1.1×10^{-1}
NW1-9	18.2	0.6	4.3	7.0×10^{-2}
NW1-10	18.6	0.0	1.9	1.2×10^{-1}
NW1-11	18.7	0.0	3.7	6.0×10^{-2}
NW1-12	22.0	0.0	4.8	8.4×10^{-2}
NW1-13	27.0	0.0	2.9	6.2×10^{-2}
NW1-14	33.5	0.0	1.7	6.6×10^{-2}
NW1-15	35.4	0.0	1.6	5.9×10^{-2}
NW1-16	40.0	0.0	1.3	5.2×10^{-2}
NW1-17	45.0	0.0	1.6	5.8×10^{-2}
NW2-1	1.1	—	13.2	1.8×10^{-2}
NW2-2	2.8	14.6	7.2	4.7×10^{-2}

NW2-3	3.7	13.1	4.8	9.4×10^{-3}
NW2-4	4.7	10.5	6.3	4.2×10^{-2}
NW2-5	5.3	8.2	3.9	1.1×10^{-2}
NW2-6	6.3	8.6	4.9	6.9×10^{-3}
NW2-7	6.6	6.2	2.3	2.3×10^{-2}
NW2-8	7.1	4.6	9.1	1.8×10^{-2}
NW2-9	8.1	3.9	3.5	2.1×10^{-2}
NW2-10	9.9	1.3	4.2	2.8×10^{-2}
NW2-11	10.8	1.0	4.6	1.1×10^{-2}
NW2-12	10.8	0.7	6.0	4.8×10^{-2}
NW2-13	11.0	1.0	5.2	4.3×10^{-2}
NW2-14	11.6	1.4	7.4	1.6×10^{-2}
NW2-15	12.5	1.2	2.4	4.3×10^{-2}
NW2-16	14.5	1.1	3.1	8.1×10^{-3}
NW2-17	15.9	0.6	5.4	4.9×10^{-2}
NW2-18	16.8	0.8	5.3	4.2×10^{-2}
NW2-19	17.7	0.6	4.8	3.9×10^{-2}
NW2-20	19.1	0.0	3.9	4.6×10^{-2}
NW2-21	19.6	0.0	3.1	2.7×10^{-2}
NW2-22	21.5	0.0	4.9	4.8×10^{-2}
NW2-23	22.4	0.0	4.2	4.4×10^{-2}
NW2-24	33.9	0.0	2.2	3.3×10^{-2}
NW2-25	40.0	0.0	1.9	3.3×10^{-2}
NW2-26	44.8	0.0	0.8	4.2×10^{-2}
NW2-27	47.6	0.0	1.0	4.8×10^{-2}
NW3-1	2.8	—	7.5	2.0×10^{-3}
NW3-2	3.9	11.8	4.7	1.8×10^{-3}
NW3-3	3.9	16.7	N/A	6.2×10^{-4}
NW3-4	5.6	9.05	4.3	4.0×10^{-3}
NW3-5	5.6	14.5	4.1	7.9×10^{-4}
NW3-6	8.5	5.4	4.4	3.6×10^{-3}
NW3-7	8.6	3.8	4.4	2.4×10^{-3}
NW3-8	12.1	4.5	—	5.2×10^{-4}
NW3-9	13.3	2.5	3.3	6.4×10^{-4}
NW3-10	19.8	0.0	1.2	1.3×10^{-3}
NW3-11	35.1	0.0	2.5	2.5×10^{-3}
NW4-1	4.4	15.1	—	4.8×10^{-4}
NW4-2	4.6	16.5	—	3.3×10^{-4}
NW4-3	4.7	17.6	—	2.8×10^{-4}
NW4-4	5.0	14.1	—	2.0×10^{-4}
NW4-5	5.1	15.1	5.3	4.5×10^{-4}
NW4-6	5.5	15.5	—	2.8×10^{-4}
NW4-7	5.8	11.5	4.6	4.4×10^{-4}
NW4-8	5.9	11.3	2.9	3.5×10^{-4}
NW4-9	6.0	13.3	—	1.8×10^{-4}
NW4-10	6.0	11.7	—	3.4×10^{-4}
NW4-11	7.0	11.1	2.3	3.5×10^{-4}
NW4-12	7.2	9.4	—	3.7×10^{-4}

NW4-13	7.8	8.0	—	2.4×10^{-4}
NW4-14	8.1	7.8	1.7	2.7×10^{-4}
NW4-15	9.4	6.4	—	3.2×10^{-4}
NW4-16	15.1	2.3	—	1.9×10^{-4}
NW4-17	15.3	1.6	2.4	1.5×10^{-4}
NW4-18	16.6	1.6	—	2.4×10^{-4}
NW4-19	21.1	0.0	—	2.5×10^{-4}

—:   Image not clear; Force not recorded

2. Additional MD simulation results

Supporting Figure S5 shows the snapshots of the PBC sample under uniaxial tension. Comparing to Fig. 3 of the paper one sees that the fracture surface is orthogonal to the tensile axis, whereas the fracture plane in the wire is inclined to the tensile axis. This is an indication that the failure of the wire has an additional shear component.

It is clear that the failure behavior in the simulation of silica glass depends strongly on the interaction potential. We therefore performed simulations with the three-body potential of Vashishta et al. and the two-body potential by van Best, Kramer and van Santen (BKS). It is important to note that both potentials lead to different defect structures in the unstrained glass samples. In particular, the BKS potential allows for the existence of over-coordinated atoms, which are not observed in the Vashishta samples. As can be seen from the stress-strain curves in Supporting Figure S6 and the snapshots in Supporting Figure S7, with the BKS potential, both the wire and the bulk sample deform in a ductile fashion. It is interesting to note that by suppressing the stress relaxation orthogonal to the tensile axis leads to brittle fracture of the PBC sample. However, these boundary conditions, also frequently used in MD simulations of glass fracture, do not represent the situation in experimental (uniaxial) tensile tests. From the bond switching (S) and loss (L) statistics (Supporting Figure S6) one sees clearly that more atoms are switching bonding partner than losing bonds. The S/L statistics during deformation can be thus used to characterize the ductility or brittleness of a given interaction potential.

10%	15%	20%	23%
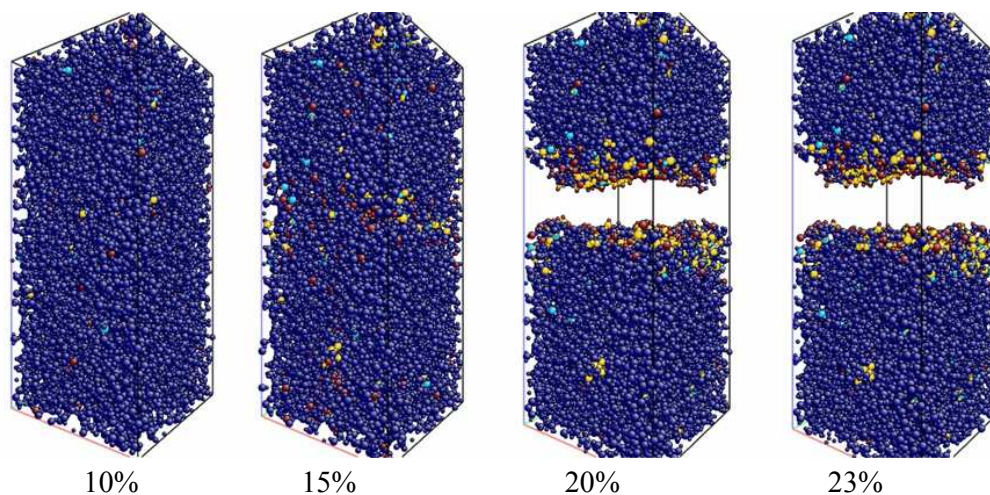
Figure S5 Snapshots from the bulk Vashishta sample at different strains. The atoms are colored according to the changes of their bonding topology: dark blue atoms have exactly the same neighbors as in the strain free initial configuration, light blue atoms have gained a bond, yellow atoms have switched bonding partners while maintaining the same coordination number, red corresponds to broken bonds.
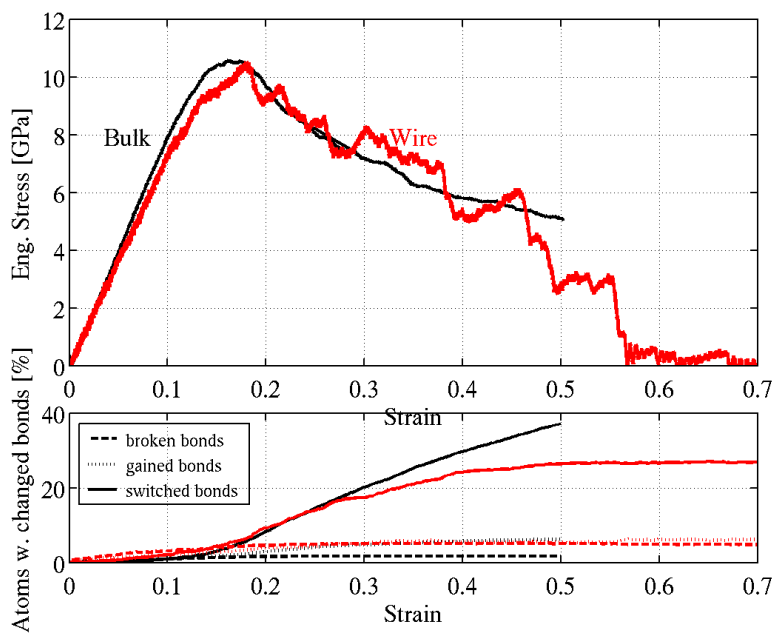
Figure S6 Stress-Strain response for the BKS sample together with the bond-change statistics.

7
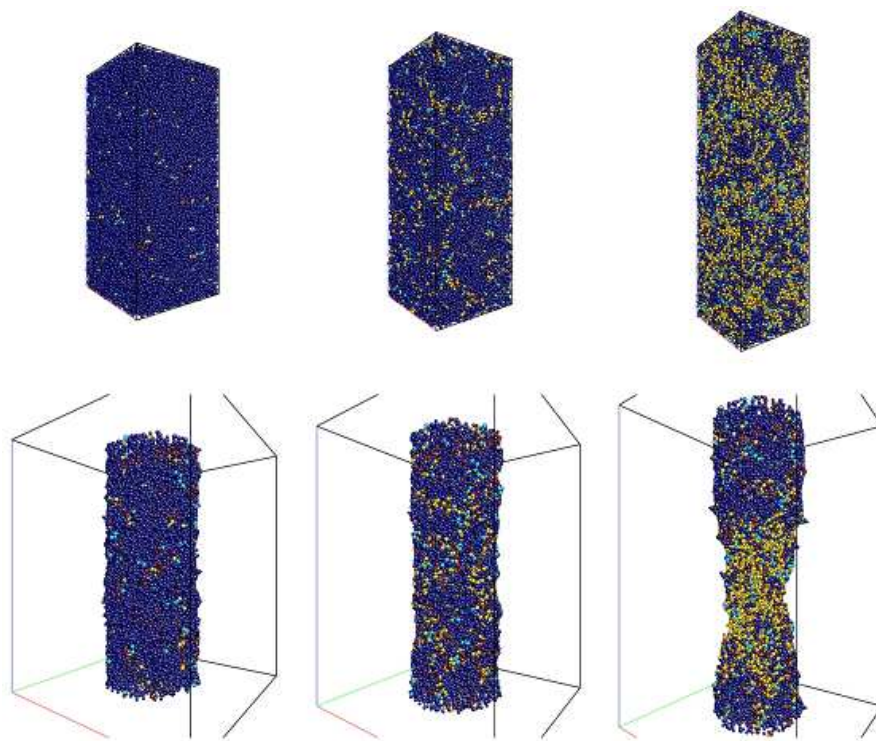
Figure S7 Snapshots of the simulations with the BKS Potential at strains of 10, 20, and 40%. See Figure S5 for the color code of the atoms.

3. Images about sample preparation
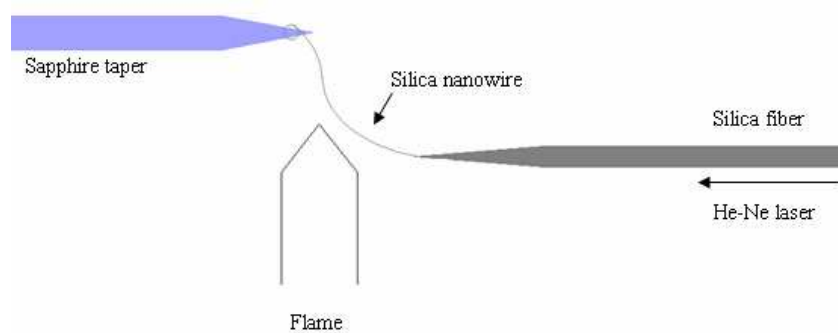
Figure S8 A schematic diagram illustrating a self-modulated taper-drawing process of ultrathin silica nanowires.
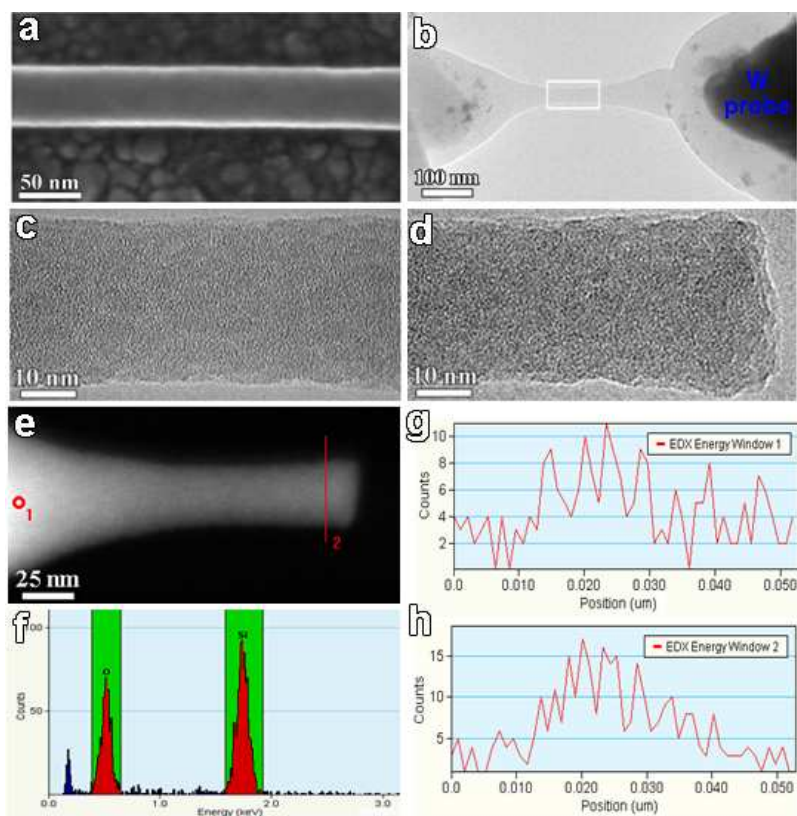
Figure S9 Structure and composition characterizations of the drawn dog-bone silica NWs. **a,** a SEM image of a 49.6 nm diameter nanowire; **b,** a TEM image of a 28.2 nm diameter dog-bone sample; **c** was taken from the white framed region of **b**; **d,** an HRTEM image of the broken part at the AFM tip side; **e**, an HAADF image of the broken part; **f,** EDS analysis at position 1 of **e**; **g** and **h** are the EDX intensity profiles along a line marked by a "2" in **e** by selecting the EDS energy window of oxygen and silicon, respectively.